Research Article Vol. 41, No. 6 / June 2024 / Journal of the Optical Society of America B 1415

Journal of the Optical Society of America B

OPTICAL PHYSICS

Strong Raman enhancement in structured colloids: localization of light

Jessica Dipold,[1] Niklaus U. Wetter,[1] Francisco C. Marques,[2] Anderson Z. Freitas,[1] Aristide Dogariu,[3] and Ernesto Jiménez-Villar[2,3,*]

[1]Instituto de pesquisas Energéticas e Nucleares, CNEN_IPEN, São Paulo, SP 05508-000, Brazil
[2]Instituto de Física "Gleb Wataghin", Universidade Estadual de Campinas, Campinas SP 13083-859, Brazil
[3]CREOL, The College of Optics and Photonics, University of Central Florida, Orlando, Florida 32816, USA
*Ernesto.jimenez@uv.es

Received 7 March 2024; revised 29 April 2024; accepted 6 May 2024; posted 6 May 2024; published 23 May 2024

Raman spectroscopy is a powerful technique for studying the interaction between light and matter. Here we show a significant enhancement of Raman emission over a broad range of pumping wavelengths from strongly scattering media comprising spatially correlated photonic structures of core–shell TiO_2@Silica scatterers mixed with silica nanoparticles and suspended in ethanol. Long-range Coulomb interactions between nanoparticles inside these photonic colloidal structures induce a correlation in the scatterers' positions (TiO_2@Silica), affecting local and global photonic properties. The anomalous enhancement in Raman signal increases as the scattering strength is increased (through either scatterer concentration or pumping wavelength); however, the signal strength continues to behave linearly with excitation power, ruling out classical nonlinear and interferential phenomena. These observations may indicate strong photon correlation in strongly localized electromagnetic modes, inducing successive photon interactions with the atoms or molecules. Aside from the fundamental relevance to understanding measurable properties in this regime of strongly localized electromagnetic modes, our demonstration of strongly enhanced Raman emission over a broad range of pumping wavelengths provides new opportunities for the development of advanced photonic materials and devices.

https://doi.org/10.1364/JOSAB.523100

1. INTRODUCTION

Raman spectroscopy has seen a fast growth in the last decades, being extensively applied to physics, chemistry, material science, and biology [1]. The Raman effect is an inelastic scattering of photons on a quantized system (molecules, crystalline structures, etc.), where the vibrational states of the system are excited by a two-photon scattering process. The Raman scattering process is characterized by very small Raman cross-sections. In general, for every 10^8 photons, only one is Raman (inelastically) scattered. Several techniques for increasing the intrinsically weak Raman scattering cross-section (Raman enhancement) by several orders of magnitude have been developed.

The two most notable techniques are surface enhanced Raman spectroscopy (SERS) and resonance Raman spectroscopy (RRS). In the RRS technique, a pumping wavelength resonant with the molecular transition of the system is used (resonant transition), which notably increases the Raman scattering cross-section. The SERS effect, which does not require a pumping photon resonant with molecular transitions (non-resonant transition), is mainly associated with the phenomenon of localized surface plasmon resonance (LSPR), which appears as a strongly localized and enhanced electromagnetic field in the vicinity of metallic nano structures [2,3]. SERS has demonstrated successful applications in biosensing [4], photodynamics [5,6], photo-thermal therapy [7], random nanolasing (spaser) [8,9], etc. The enhancement factor of the Raman signal, G_R, due to SERS and mediated by LSPR is defined as

$$G_R = \frac{|E_{\mathrm{Loc}}(\omega_P)|^2}{|E_0(\omega_P)|^2} \times \frac{|E_{\mathrm{Loc}}(\omega_R)|^2}{|E_0(\omega_R)|^2} \approx \frac{|E_{\mathrm{Loc}}(\omega_P)|^2 \times |E_{\mathrm{Loc}}(\omega_R)|^2}{|E_0|^4},$$

where ω_P and ω_R are the pumping and emission Raman frequencies, respectively. E_{Loc} is the locally enhanced electromagnetic field resulting from the light localization, at the pumping (ω_P) and emission Raman (ω_R) frequencies. E_0 represents the electromagnetic field of the incoming laser wave. If $\omega_P \approx \omega_R$, a fourth power dependency of the SERS enhancement occurs [10]. LSPR excitation or a plasmonic effect is attributed to the collective oscillation of the electron cloud in the metal nanoparticle, which, in turn, induces significant absorption losses by the inelastic electronic scattering. LSPR is a

particular case of localization of light (strongly localized electromagnetic modes) in the vicinity of metallic nano structures. Unlike the plasmonic effect, localization of light in a structured dielectric colloid does not implicitly entail absorption losses, which represents an important advantage.

Localization of light delves into fundamental concepts of physics; however, it has proven elusive in dielectrics scattering media [11,12], which has led to extensive debate [13–16] raising an obligatory question: what scientific-technological significance could this controversial phenomenon of light localization bring? The strategy used in these dielectrics scattering media was to increase the scattering concentration by reducing the separation between scatterers in order to reach the Ioffel-Regel criterion ($kl_T \sim 1$), where $k = 2\pi/\lambda$ and l_T are the wave number and transport mean free path, respectively. However, a decrease in the separation between scatterers favors the near field dipole-dipole coupling, which was conjectured to prevent the localization of vector waves (light) [17].

An additional strategy for localization of light that consists of inducing a correlation in the scatterers' positions (structured scattering medium) was suggested early by John by introducing defects into a photonic crystal [18]. The tendency towards localization by correlated long-range hopping in higher dimensional systems, called "correlation-induced localization," has been shown theoretically by Kravtsov and coworkers, demonstrating the universality of this phenomenon [19]. A renormalization of the absorption coefficient (enhanced absorption) was predicted to occur in a disordered scattering medium at the mobility edge [20], which was attributed to the strong photon correlation within localized states (strongly localized electromagnetic modes) [21]. Recently, Dal Negro and co-workers showed also theoretically a strongly enhanced light-matter coupling at localization transition induced by the engineering of correlations in photonic media [22,23].

Engineered or correlated disorder in photonic assemblies can yield anomalous and impactful optical phenomena such as unidirectional invisibility, enhanced light-matter interaction and single mode lasing. Detailed reviews on this topic have been published elsewhere [24–27].

In the last years, we have been studying the transport of light, random lasing, and the light-matter interaction in a colloidal system composed by core–shell TiO_2@Silica nanoparticles (NPs) suspended in ethanol [28–36]. We showed that the correlation in the scatterers' positions [35–37], due to the long-range Coulomb interaction, induces a significant enhancement of the light-matter interaction [30,35]. Strong enhancement of the Raman signal [35] and absorption [30] per TiO_2@Silica particle have been observed in this hyperuniform colloidal-photonic structure.

It is well known that the inelastic scattering processes (absorption or nonlinear phenomena) have resulted in important obstacles for localization of light (strongly localized electromagnetic modes) [13,14]. Thus, it is expected that evidence for localization of light could be provided by non-resonant Raman scattering in TiO_2@Silica plus silica NP suspensions with a low enough sensitivity to not affect interferential processes.

Here, we report experiment on colloidal systems comprising silica NPs of 20 nm diameter with filling fractions (FF_{SiO_2}) of 0.75% and 1.5% that were mixed to suspensions of TiO_2@Silica with filling fractions (FF_{TiO_2}) ranging from 0.26% up to 12.1%. See details in Section 2 and Appendix A. The Raman signature of the TiO_2 core (rutile, 410 nm mean diameter) was monitored as a function of FF_{TiO_2} (from 0.26% up to 12.1%). The Raman signal was collected by using two objectives (60× and 50×) with different numerical apertures (1.41 and 0.55), respectively, which can provide information on the influence of pumping volume and pumping incidence angle on the Raman signal.

2. MATERIALS AND METHODS

TiO_2@Silica NPs, synthesized by an improved Stöber method [30] (see Appendix A), were dispersed in an ethanol (HPLC) solution at different FF_{TiO_2} ranging from 0.26% up to 12.1%. Additionally, silica NPs at $FF_{SiO_2} = 0.75\%$ and 1.5% were added to these TiO_2@Silica NP suspensions. The TiO_2@Silica NPs used in the current experiments are the same as those used in our previous reports [30–36]. TEM images, a mapping EELS (electron energy loss spectroscopy) (Si), and energy dispersive X-ray fluorescence (ED-XRF) of the core–shell TiO_2@Silica NPs were performed and reported in our previous work [30]. The mass percentage ratio (Ti/Si), determined by ED-XRF, was Ti_{72}/Si_{28}, which allows estimating a silica shell thickness of $\sim 40 - 45$ nm. Diffraction patterns from the TiO_2@Silica suspensions showing the correlation of the scatterers' positions can be found in our previous works [36,37]. TEM images of core–shell TiO_2@Silica NPs and a schematic diagram of the Raman measurement are shown in Fig. 1. The silica NPs enhance the colloidal electric (Coulomb) interaction, since silica NPs, located between the TiO_2@Silica NPs, would act like pivots or bridges for the Coulomb interaction between TiO_2@Silica NPs, reducing the effective distance of interaction between the latter. A theoretical description of the particle interaction and colloidal crystallization can be found in Appendix A and in our previous works [35–37].

A Micro-Raman (LabRAM HR Evolution, Horiba Scientific) with four CW lasers (473 nm, 25 mW; 532 nm, 50 mW; 633 nm, 17 mW; and 785 nm, 100 mW) as excitation sources was used for Raman scattering measurements. The experimental setup is the same as described previously [35]. To study the influence of pumping volume (spot size and deep of focus) and pumping and collection angle on the Raman signal, Micro-Raman measurements were done using two objectives, an oil-immersion Olympus 60× objective with a high numerical aperture of 1.41, which translates into a collection depth into the samples of $d_B \approx 1.2\ \mu$m, and another, Leica 50× objective with numerical aperture 0.55 and collection depth of $d_B \approx 2.67\ \mu$m. The collection depth (d_B) was calculated through $d_B = \frac{\lambda * n^2}{NA}$, where λ is the pumping wavelength, n is the refractive index of the medium, and NA is the numerical aperture of the objective. For both objectives (60× and 50×), a glass slide of 170 μm thickness was used to cover the samples and a total of four spectra, collected from different points, were recorded for each sample. The position of the focal plane of the objective relative to the sample surface was chosen such that the maximum Raman signal was obtained, which means that the effective depth of pumping and collection into the

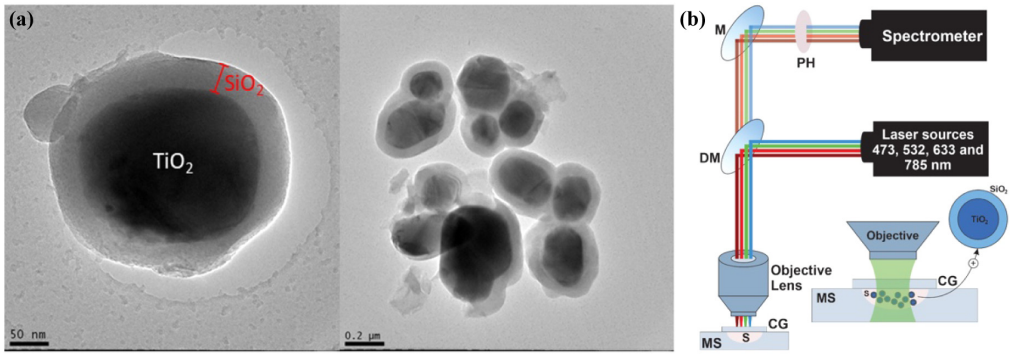

Fig. 1. (a) Images of the TiO_2@Silica NPs via transmission electron microscopy (TEM) show the SiO_2 shell around the TiO_2 core. (b) Experimental setup for collecting the Raman scattering signal using four different pumping lasers, where PH = pinhole, M = mirror, and DM = dichroic mirror. Sample (S) is irradiated with four different pumping wavelengths (laser sources). A quartz sample holder (MS) supporting 80 μl of the sample (S) is covered with a BK7 cover glass (CG) of 170 μm thickness. Each laser is focused separately with the objective lens in the studied sample right between the cover glass and the suspension. To the right, a zoom of the focusing of the objective and a TiO_2@Silica schematic.

sample could be slightly less than the depth of focus of the objective (d_B).

The samples are stirred before each measurement and the Raman collection is performed during a time shorter than 1 min. After several minutes the Raman signal starts to decrease slowly, which could be a consequence of an effective FF_{TiO_2} decrease close to the sample-cover slip interface, probably due to the gravity effect. In order to not saturate the detector, the pumping and collection time is decreased from 10 s at $FF_{TiO_2} = 0.26\%$ down to 0.1 s at $FF_{TiO_2} = 12.1\%$. The Raman signal increases linearly with pumping and collection time as expected, ruling out a thermophoretic effect in this range of processing time and pumping power.

3. RESULTS

The results are divided into three main sections. In the first section (Raman signal study with the 60× objective, high numerical aperture), the Raman signal is collected by pumping the sample (TiO_2@Silica suspensions plus silica NPs) with the 532 nm laser (50 mW with power fluctuation ±1%) using the oil-immersion 60× objective (NA = 1.41) and a glass slide to cover the samples. The depth of pumping and collection is $d_B \approx 1.2$ μm and the cone half-angle of the incident pump beam and the Raman signal collection is ∼±68°. The Raman signals for the TiO_2@Silica (without silica NPs) and TiO_2 (without silica shell) suspensions in ethanol are shown for comparison purposes. In the second section (Raman signal study with the 50× objective, low numerical aperture), the Raman study was performed with the same 532 nm laser as the excitation source on the same TiO_2@Silica suspensions with the addition of silica NPs using the 50× objective (NA = 0.55) and the same glass cover slide, which translates into a depth of pumping and collection of $d_B \approx 2.67$ μm. The cone half-angle of pumping and collection is considerably smaller, ∼±21.2°. The Raman signal, collected with the 60× objective (NA = 1.41), is shown for comparison. Illustrations of pumping and Raman signal collection at the sample-slide interface using the two objectives (60× and 50×) are shown in Appendix A (Fig. 5). In the third section (Raman signal study with different pumping wavelengths), the Raman signal was studied with different pumping wavelengths, for two specific FF_{TiO_2} (4.8% and 8.8%). The Raman signal was studied using the 50× objective and four pump lasers with wavelengths of 473 nm, 532 nm, 633 nm, and 785 nm.

A. Raman Measurements with a High Numerical Aperture Objective

Raman signals were measured from TiO_2@Silica suspensions containing various amounts of silica nanoparticles. Typical Raman spectra, collected from the TiO_2@Silica suspensions with FF_{TiO_2} of 0.26%, 1.35%, and 12.1% and silica NPs at $FF_{SiO_2} = 1.5\%$, are shown in Appendix A (Fig. 6). Two strong Raman peaks located at around 445 and 608 cm^{-1} assigned to the E_g and A_{1g} modes of rutile are observed.

Figure 2(a) shows the intensity of the E_g peak at 445 cm^{-1} as a function of FF_{TiO_2}. The intensity of this Raman peak, measured on similar TiO_2@Silica suspensions but without silica NPs and for TiO_2 without silica shell suspensions, was scaled and plotted for comparison purposes. As shown for all TiO_2@Silica concentrations, the Raman intensity increases quicker than linearly once the FF_{TiO_2} is increased above a specific value ($FF_{TiO_2(onset)}$). This reveals an anomalous enhancement of emission efficiency per particle. Conventionally, the Raman signal must be proportional to both the emitter concentration (FF_{TiO_2}) and excitation intensity. This is evident in the case of the TiO_2 suspension without the silica shell, for which the Raman signal increases linearly with FF_{TiO_2} as expected. This enhancement of the Raman signal per particle is illustrated in Fig. 2(b) as a function of FF_{TiO_2}. The measured enhancement in the TiO_2@Silica suspensions with the addition of silica NPs is higher than that without silica NPs. Moreover, for TiO_2@Silica suspensions with silica NPs, $FF_{TiO_2(onset)}$ is lower than without silica NPs. For TiO_2@Silica suspensions with silica NPs, this enhancement of the Raman signal is observed above $FF_{TiO_2(onset)} = 0.54\%$, whereas for TiO_2@Silica suspensions without silica NPs, $FF_{TiO_2(onset)} = 1.06\%$. Below $FF_{TiO_2(onset)}$, Raman intensity shows the expected linear behavior in FF_{TiO_2}. The $FF_{TiO_2(onset)}$

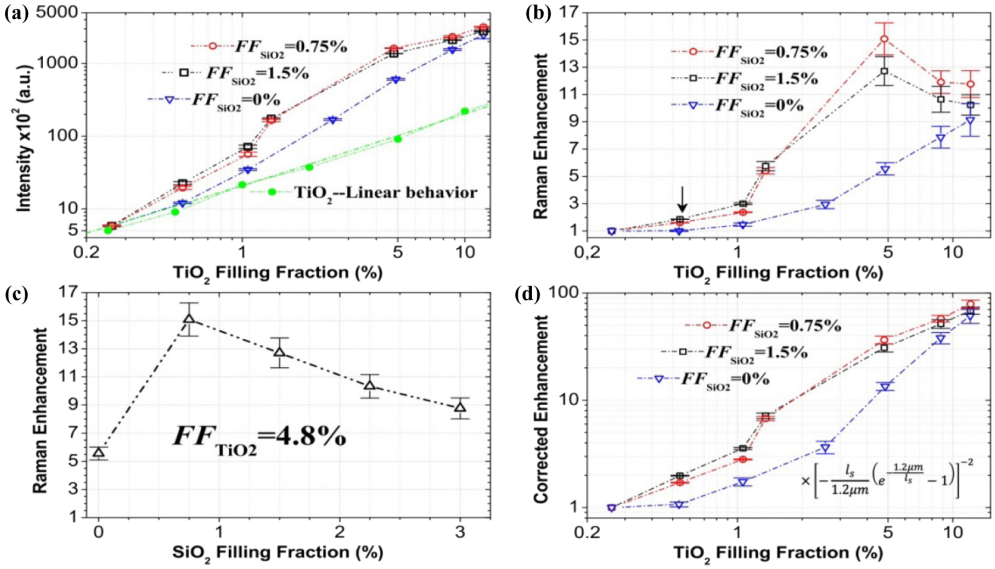

Fig. 2. Enhancement of the Raman signal for TiO_2@Silica suspensions in ethanol with and without silica NPs collected with a 60× oil-immersion objective of numerical aperture of NA = 1.41. (a) For TiO_2@Silica suspensions with FF_{SiO_2} of: 0%, 0.75%, and 1.5%, the intensity of the experimentally measured Raman peak (E_g; 445 cm^{-1}) as a function of FF_{TiO_2} increases quicker than the expected linear behavior (TiO_2 suspensions, green dots). (b) Intensities of the Raman peak normalized by FF_{TiO_2} (Raman signal per particle) show an enhancement above $FF_{TiO_2} = 0.54\%$ (FF_{TiO_2} onset represented by black arrow) for FF_{SiO_2} of 0.75% and 1.5%. (c) For $FF_{TiO_2} = 4.8\%$, the Raman enhancement as a function of FF_{SiO_2} (0%, 0.75%, 1.5%, 2.25%, and 3%) reveals a decrease as FF_{SiO_2} is increased above $FF_{SiO_2} = 0.75\%$. (d) Raman enhancement corrected by the pumping and collection depth (Raman signal was scaled by the inset equation). The error bars represent the maximum and minimum values of the Raman intensity peak.

criterion was taken at the FF_{TiO_2} where the Raman signal increases quicker than the expected linear behavior in FF_{TiO_2}.

We note that, with the addition of silica NPs, $FF_{TiO_2(onset)}$ could be even lower than $FF_{TiO_2} = 0.54\%$, but to confirm that, the Raman signal would have to be measured at $FF_{TiO_2} < 0.26\%$. However, because of the weak Raman signal at $FF_{TiO_2} < 0.26\%$, the measurement and the extracted enhancement curve become inaccurate. If $FF_{TiO_2(onset)}$ is a lower value, the calculated Raman enhancement would be even stronger. We observe that for all TiO_2@Silica suspensions (FF_{TiO_2}), the Raman signal increases linearly with the pumping intensity as expected. Therefore, a classical nonlinear phenomenon sustained by the increased probability of simultaneous multi-photons interaction cannot explain this enhanced Raman signal in FF_{TiO_2}.

This phenomenon can be attributed to strong photon correlation within strongly localized electromagnetic modes (localized states), which are spatially densely overlapped, leading to an increased probability of sequential photon interactions. This latter could be understood as photons trapped within localized states successively interacting with the same atoms or molecules, i.e., the successive polarization of valence electrons both to virtual states (non-resonant) and to metastable states (resonant transitions), which gives rise to an enhanced light-matter interaction [22,38]. This increase of Raman enhancement in FF_{TiO_2} is attributed to an increase in the densities and Q-factors of these strongly localized electromagnetic modes as FF_{TiO_2} is increased. The stronger enhancement of the Raman signal for TiO_2@Silica NPs suspensions with the addition of silica NPs can be attributed to an increase of the correlation in the scatterers' positions (TiO_2@Silica NPs), due to stronger Coulomb interaction between scatterers caused by the presence of the silica NPs. A stronger correlation in the scatterers' positions could be understood as an increase in the range of order extension or the size of ordered or structured clusters, which should induce higher densities and Q-factors of the localized electromagnetic modes (localized states).

The presence of silica NPs between the TiO_2@Silica NPs (scatterers) must enhance the effective Coulomb interaction between all NPs (TiO_2@Silica & Silica) within the colloid, since the effective distance for Coulomb interaction is reduced. For $FF_{TiO_2} < 4.8\%$, the enhancement of the Raman signal for $FF_{SiO_2} = 1.5\%$ is higher than that for $FF_{SiO_2} = 0.75\%$, which can be associated to stronger correlation in the scatterers' positions as a consequence of stronger Coulomb interaction (higher FF_{SiO_2}). However, for $FF_{TiO_2} \geq 4.8\%$, this behavior is reversed, which could be attributed to higher residual absorption for $FF_{SiO_2} = 1.5\%$ in comparison with $FF_{SiO_2} = 0.75\%$. This behavior would be appreciable when FF_{TiO_2} is increased, due to an increase of the absorption enhancement in FF_{TiO_2} (increase of the densities and Q-factors of localized states) [30]. Notice that the surface of silica NPs can be an important source of residual absorption, due to the dangling bonds. In order to corroborate this hypothesis, the Raman signal for $FF_{TiO_2} = 4.8\%$ was recorded as a function of FF_{SiO_2} (0%, 0.75%, 1.5%, 2.25%, and 3.0%).

Figure 2(c) shows the enhancement of the Raman signal for $FF_{TiO_2} = 4.8\%$ as a function of FF_{SiO_2}. The strongest enhancement of the Raman signal is revealed for $FF_{SiO_2} = 0.75\%$. A further increase of FF_{SiO_2} leads to a monotonic decrease of the Raman signal enhancement, which effectively could be caused by an appreciable increase of residual absorption as

FF_{SiO_2} is increased above $FF_{SiO_2} = 0.75\%$ for $FF_{TiO_2} = 4.8\%$, possibly reducing the Q-factors of localized states. We must highlight that the scattering lengths (l_s), calculated by Mie theory considering a random scattering medium, are practically the same with and without addition of silica NPs for all FF_{SiO_2}. This is expected since the diameter (20 nm) and refractive index (1.45) of silica NPs are considerably lower than those of the TiO_2@Silica NPs, which have a TiO_2 core of 410 nm and refractive index of 2.8, respectively. On the other hand, in our previous work [35], we showed that l_s values for the TiO_2@Silica colloidal suspensions in water and ethanol are similar, as expected by Mie theory considering disordered scattering media. However, the TiO_2@Silica Coulomb interaction is appreciably different in these suspensions (water and ethanol), which showed that l_s is insensitive to the Coulomb interaction in the studied range, i.e., it seems to be insensitive to the structure's order. We remark that the experimental setup (oil-immersion 60× objective with NA = 1.41) allows a collection depth of $d_B \approx 1.2$ μm. Therefore, in order to have a better comparison of the enhancement as a function of FF_{TiO_2}, a correction of the Raman intensity considering the pumping and collection depths is required, particularly for shorter scattering lengths ($< d_B = 1.2$ μm). Thereby, the measured Raman signal is divided by $[-\frac{l_s}{d_B}(e^{-\frac{d_B}{l_s}} - 1)]^2$ for each sample (see Appendix A). The above correction is obtained considering an exponential decrease in depth of the Raman pumping and collection intensity (see Appendix A). However, at the transition regime of localization, pumping intensity should decay quicker than exponential as we have shown in our previous work [30], which implies that the above correction is an approximation.

Nevertheless, because pumping and collection depth is small in comparison with l_s, the expected deviation from the exponential decay at this depth should be small, being only appreciable for the highest FF_{TiO_2} values. In any case, a quicker exponential decay would imply a Raman enhancement that would be even stronger than the one extracted by the above correction. For pumping and collection, the light reflected at the oil-slide (glass) interface was not considered because of index matching. Figure 2(d) shows the enhancement of the Raman signal in FF_{TiO_2} after correcting for the pumping and collection depths. As can be observed, for $FF_{SiO_2} = 0.75\%$, the Raman enhancement factor increases monotonically in FF_{TiO_2} and it reaches 80 for $FF_{TiO_2} = 12.1\%$, which makes this colloidal system a highly sensitive detection tool.

An apparent saturation of the Raman enhancement is observed for $FF_{TiO_2} \geq 4.8\%$ ($FF_{SiO_2} = 0.75\%$ & 1.5%). This behavior could be associated with the losses by residual absorption and/or internal reflection experimented by emitted Raman photons at the sample-slide interface, which would become appreciable at $FF_{TiO_2} \geq 4.8\%$ due to the stronger enhancement of the absorption (expected) and possibly the refractive index ($FF_{TiO_2} \geq 4.8\%$). Notice that this oil-immersion 60× objective with the high numerical aperture of NA = 1.41 allows pumping the sample and collecting the Raman signal at very high angles, which could cause an increase of residual absorption and/or internal reflection as a consequence of the excitation of localized modes with higher Q-factors. A similar effect has been shown in our previous works [33,34], where the internal reflection and residual absorption near the input surface increase as the incidence angle is increased. In order to examine the Raman enhancement in FF_{TiO_2} and the influence on it of the pumping and collection angle, the Raman signal as a function of FF_{TiO_2} was recorded with the 50× objective of lower numerical aperture, NA = 0.55, whose solid angle of collection is considerably lower than that of the 60× objective (NA = 1.41). Illustrations of pumping and collection of the Raman signal with both objectives (60× and 50×) can be found in Appendix A (Fig. 5).

B. Raman Measurements with a Low Numerical Aperture Objective

Comparing Fig. 3(a) to Fig. 2(a) shows that, like the measurement with the higher numerical aperture (NA = 1.41), the intensity of the Raman peak (E_g; 445 cm^{-1}) also increases quicker than linearly as FF_{TiO_2} is increased above $FF_{TiO_2(onset)} = 0.54\%$, revealing an enhancement of the Raman signal per particle. However, the Raman signal is lower than that collected with the 60× objective (Fig. 2), which is explained by three main factors: (i) the objective collection angle is reduced from ±68° down to ±21.2°, (ii) increase of pumping and collection depth ($d_B = 2.67$ μm) to values larger than the scattering length of most samples, and (iii) increase of reflected light at the air-slide interface (no index matching).

Figure 3(b) shows the enhancement of the Raman signal per particle, extracted from measurements without corrections, as a function of FF_{TiO_2}. Figure 3(c) shows the enhancement of the Raman signal corrected by the pumping and collection depth and the reflected light at the air-glass slide interface (for incoming and outgoing light), scaled by the following equation:

$$\left[-\frac{l_s}{2.67\ \mu m}\left(e^{-\frac{2.67\ \mu m}{l_s}} - 1\right)\right]^{-2} \langle 1 - \mathrm{Ref_{CM}}^{-1} \rangle,$$

where Ref_{CM} is the reflection coefficient averaged over the pumping and collection cone angle at the air-glass slide interface (see Appendix A). The estimated Raman enhancement after corrections reaches 250 for $FF_{TiO_2} = 12.1\%$ and $FF_{SiO_2} = 0.75\%$ [Fig. 3(c)], which is appreciably higher than that of the 60× objective with NA = 1.41 [80 times, Fig. 2(d)]. The latter could be originated by a reduction in the losses due to internal reflection when using this 50× objective (NA = 0.55). Note that the incident and collection cone angle is appreciably lower (±21.2°) than that of the previous measurements with the 60× objective (±68°). In order to better understand the influence of the objective's numerical aperture, the corrected Raman enhancement for the samples with $FF_{SiO_2} = 0.75\%$, measured with both objectives (NA = 1.41 and NA = 0.55), are displayed in Fig. 3(d). For $FF_{TiO_2} \geq 4.8\%$, the enhancement of the Raman signal obtained with the 60× objective (NA = 1.41) is slightly stronger than that of the 50× objective (NA = 0.55), which is expected since localization near the sample input surface must increase with the incident angle (higher densities and Q-factors of localized states) [33,34].

However, for $FF_{TiO_2} \geq 4.8\%$, this behavior is reversed, which could be associated with an increase of the losses by the enhanced residual absorption and/or internal reflection for measurements with NA = 1.41 in comparison with NA = 0.55. The above result ($FF_{TiO_2} \geq 4.8\%$) is expected since localized states with higher Q-factors can be excited with NA = 1.41 (higher incident angles). Therefore, if losses are negligible for

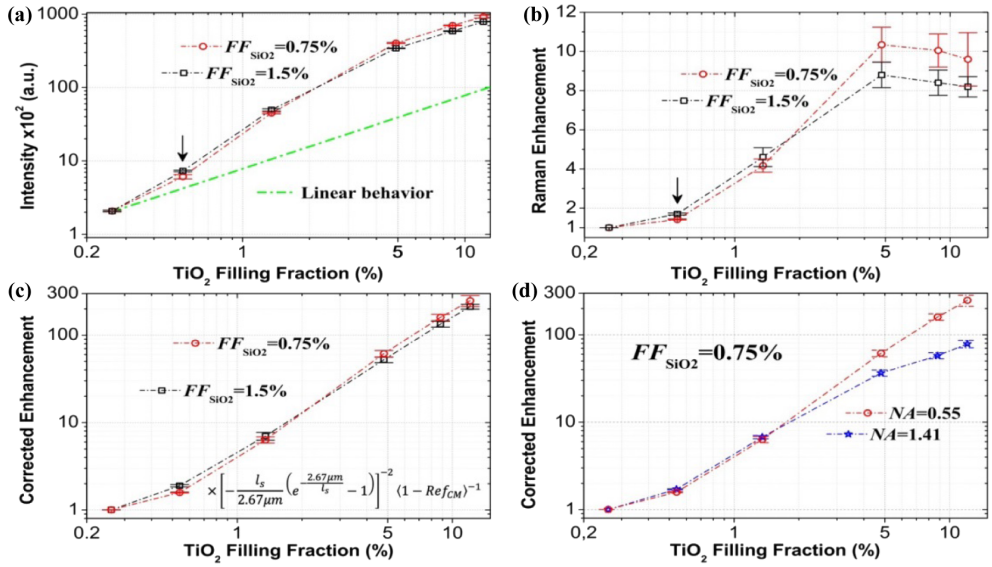

Fig. 3. Enhancement of the Raman signal for TiO_2@Silica suspensions in ethanol with silica NPs collected with the 50× objective with numerical aperture of NA = 0.55. (a) For both FF_{SiO_2} of 0.75% and 1.5%, the intensity of the Raman peak (E_g; 445 cm^{-1}) measured as a function of FF_{TiO_2} increases quicker than the expected linear behavior (green line). (b) Intensities of the Raman peak normalized by FF_{TiO_2} (Raman signal per particle) show an enhancement above $FF_{TiO_2} = 0.54\%$ (FF_{TiO_2} onset represented by black arrow). (c) Raman enhancement corrected by the pumping and collection depth and the reflection at the air-slide (glass) interface (using equation shown in inset). (d) For $FF_{SiO_2} = 0.75\%$, corrected Raman enhancements, measured with NA = 1.41 (blue stars) and NA = 0.55 (red circles), are compared. The error bars correspond to the maximum and minimum values of the Raman intensity peak.

$FF_{TiO_2} \geq 4.8\%$, stronger enhancement of the Raman signal is expected for NA = 1.41 in comparison with NA = 0.55. The increase of these losses would be appreciable as FF_{TiO_2} is increased ($FF_{TiO_2} \geq 4.8\%$), due to the enhanced absorption [20,30] and the possible increase of the effective refractive index in FF_{TiO_2}. In fact, a saturation in the enhancement of the Raman signal at $FF_{TiO_2} \geq 4.8\%$ is clearly appreciable for the higher numerical aperture (NA = 1.41), which, effectively, could indicate that the losses of the Raman signal, particularly for $FF_{TiO_2} \geq 4.8\%$, increase as the objective's numerical aperture is increased. A detailed Raman study is called for in order to understand in depth the influence of pumping and collection angles on this anomalous enhanced light-matter interaction in this engineered-hyperuniform scattering medium.

For all $FF_{TiO2} > FF_{TiO_{2(onset)}}$, a monotonic increase of the Raman signal enhancement is observed in FF_{TiO_2} using both objectives. We remark that a classical interferential phenomenon cannot explain the monotonic increase of the Raman enhancement in FF_{TiO_2}, since it would make the Raman enhancement strongly sensitive to the interparticle distance (constructive and destructive interference), which is directly linked to FF_{TiO_2}. Nevertheless, to clearly rule out a classical interferential phenomenon, a study of the Raman signal covering a wide range of pumping wavelengths is imperative.

C. Raman Measurements with Different Pumping Wavelengths

In order to rule out a classical interferential phenomenon, the Raman signal for two specific FF_{TiO_2} of 4.8% and 8.8% and $FF_{SiO_2} = 0.75\%$ was measured by pumping the samples (50× objective) with four different wavelengths (473 nm, 532 nm, 633 nm, and 785 nm). The scattering strength, calculated by

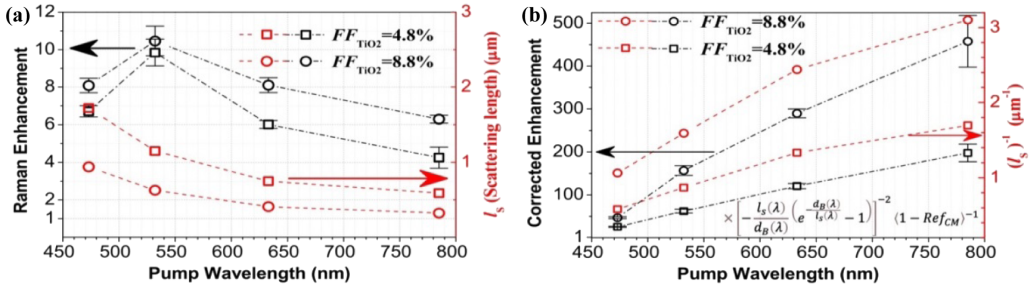

Fig. 4. (a) For FF_{TiO_2} of 4.8% (open squares) and 8.8% (open circles), Raman enhancement (left-black axis) and scattering length (l_s; right-red axis) as a function of the pumping wavelength. (b) For FF_{TiO_2} of 4.8% (open squares) and 8.8% (open circles), (left-black) corrected Raman enhancement (using equation shown in inset) and (right-red) l_s^{-1} as a function of the pumping wavelength. The error bars correspond to the maximum and minimum values of the Raman intensity peak. The dashed and dotted lines (black and red) are only to connect the experimental and theoretical points.

Mie theory for $FF_{TiO_2} = 4.8\%$, is displayed as a function of the wavelength in Fig. 7(a) (Appendix A).

Figure 4(a) shows, for FF_{TiO_2} of 4.8% and 8.8%, (left-black), the enhancement of the Raman signal per particle, extracted from measurements without corrections, and (right-red) the scattering lengths (l_s), determined from Mie theory for each pumping wavelength. A decrease of l_s is observed as the pumping wavelength increases between 473 nm, 532 nm, 633 nm, and 785 nm. Figure 4(b) shows (left-black) the enhancement of the Raman signal, corrected by the pumping and collection depth and the reflected light at the air-glass slide interface, and (right-red) l_s^{-1} (scattering strength), as a function of the pumping wavelength. The collected Raman signal was scaled as $[-\frac{l_s(\lambda)}{d_B(\lambda)}(e^{-\frac{d_B(\lambda)}{l_s(\lambda)}} - 1)]^{-2}\langle 1 - \mathrm{Ref_{CM}}\rangle^{-1}$, where both $d_B(\lambda)$ and $l_S(\lambda)$ are dependent on the pumping wavelength. As clearly observed, the rise of the corrected Raman enhancement as pumping wavelength is increased corresponds with the growth of the scattering strength (l_s^{-1}), which represents strong additional evidence of localization of light. Note that, according to theoretical prediction, localization of light must increase (higher densities and Q-factors of localized states) as scattering strength augments.

Furthermore, this Raman enhancement behavior in l_s^{-1} excludes a classical or simple interferential phenomenon. Further studies on the enhancement of the Raman signal and refractive index are called for in order to deepen the understanding of the light-matter interaction and their consequences in this engineered-hyperuniform scattering medium.

4. CONCLUSION

A strongly enhanced Raman signal is observed in the TiO_2@Silica suspension in ethanol, being considerably stronger when silica NPs (20 nm diameter) are added. This finding is attributed to a stronger long-range Coulomb interaction between TiO_2@Silica NPs (scatterers) by the presence of silica NPs, which act like pivots or bridges for the interaction between TiO_2@Silica NPs. The latter leads to stronger correlation of the scatterers' positions, which, in turn should increase the densities and Q-factors of strongly localized electromagnetic modes (localized states).

An increase in FF_{SiO_2} from $FF_{SiO_2} = 0.75\%$ up to $FF_{SiO_2} = 1.5\%$ leads to an increase in the enhancement of the Raman signal. However, when FF_{TiO_2} is increased above 1.35%, this behavior is reversed (Raman enhancement is higher for the lower $FF_{SiO_2} = 0.75\%$), which we attributed to an increase in the losses by residual absorption ($FF_{SiO_2} = 1.5\%$) due to the dangling bonds present on the silica NPs' surface that can become a significant source of residual absorption when $FF_{TiO_2} \geq 4.8\%$. Raman measurements performed with two objectives of NA = 1.41 and 0.55 showed stronger enhancement of the Raman signal for the larger NA of 1.41 when $FF_{TiO_2} < 4.8\%$, which was attributed to the excitation of localized states with higher Q-factors (higher pumping and collection angles). However, when $FF_{TiO_2} \geq 4.8\%$, this behavior is reversed, which we attributed to an increase in the losses by both residual absorption and internal reflection at the sample-glass interface. Note that when the objective numerical aperture is increased (NA = 1.41), localized states with higher pumping and collection angles must be excited (higher Q-factors), leading to stronger enhancement of absorption and, possibly, of the effective refractive index.

A classical interferential phenomenon was ruled out by studying the Raman signal as a function of the scattering strength for different pumping wavelengths. Keeping FF_{TiO_2} constant, a correspondence in the increase of the Raman enhancement and scattering strength is observed, which represents strong evidence of localization of light. Note that a classical interferential phenomenon would make the Raman enhancement strongly sensitive to the pumping wavelength and interparticle distance, this latter being directly linked to FF_{TiO_2}. In contrast, a monotonic increase in the enhancement of the Raman signal is observed as scattering strength increases (through either pumping wavelength or FF_{TiO_2}). We propose that the anomalous nonlinear phenomenon (strongly enhanced Raman signal), shown in this work, would be induced by the increased probability of sequential photon interactions (successive polarization of valence electrons to virtual states) within these strongly localized electromagnetic modes, due to strong photon correlations.

Finally, the considerable benefit of sequential photon interaction is that it emerges even at a very low intensity of the incoming electromagnetic field, i.e., there is no threshold for this phenomenon. The findings presented here open an avenue for designing and manufacturing advanced photonics devices.

APPENDIX A

A.1. Materials

Ethanol alcohol HPLC with spectroscopic grade purity was supplied by MERCK, tetra-ethyl-ortho-silicate (TEOS) was supplied by Sigma-Aldrich, and the ammonia P.A. was supplied by MERCK. The titanium dioxide (TiO_2) with a rutile crystal structure was acquired from DuPont Inc. (R900). The TiO_2 grains have an average particle diameter of 410 nm with a polydispersity of 25%. TiO_2 nanoparticles were coated with a silica shell of ∼40 nm thickness via the Stöber method. In the first stage, 5 g of TiO_2 NPs were dispersed in 500 ml of absolute ethanol. This suspension was placed in an ultrasound bath for 20 min to disperse the particles and 6.67 mL of ammonia and 10 mL of TEOS were added. The TEOS and commercial ammonia (NH_4OH 28%-30%) were added alternately in 100 portions of 100 µl and 220 µl, respectively. The synthesized TiO2@Silica nanoparticle suspension was centrifuged at 3000 g for 20 min and the pellet was dried in an oven at 70°C for 12 h. Transmission electron microscopy (TEM) and energy dispersive X-ray fluorescence (ED-XRF) of the same, as-synthesized core–shell TiO_2@Silica NPs were performed and reported in our previous work [30]. The mass percentage ratio (Ti/Si), determined by ED-XRF, was Ti_{72}/Si_{28}. The powder of TiO_2@Silica NPs was re-dispersed in ethanol at different TiO_2 filling fractions (FF_{TiO_2}). Suspensions were prepared with FF_{TiO_2} of 0.26%, 0.54%, 1.35%, 4.8%, 8.8%, and 12.1%. Additionally, silica NPs of 20 nm diameter, acquired from SSNano, were added in the TiO_2@Silica NPs suspensions at SiO_2 filling fraction (FF_{SiO_2}) of 0.75% and 1.5%.

A.2. Long-Range Coulomb Interaction between Scatterers

According to the classical theory of Derjaguin-Landau-Verwey-Overbeek (DLVO) [39], the pair-wise particle interaction arises from the interplay of attractive van der Waals forces (F_{attr}) and repulsive Coulomb forces (F_{rep}, double layer force) screened by the Debye-Hückel ions' cloud. The modulus of both interaction potentials (electrostatic repulsion, U_{elec}, and the van der Waals attraction, U_{vdw}) increases when the separation between particles decreases. The total interaction potential between two particles (UTDLVO) can be expressed as the sum of the electrostatic repulsion (U_{elec}) and the van der Waals attraction (U_{vdw}): $\mathrm{UTDLVO} = U_{elec}(r) + U_{vdw}(r)$, where r is the distance (center-to-center) between two particles of radii a ($r = h + 2a$, with h being the distance between the surfaces). Depending on the particle size and the thickness of the double layer, the electrostatic repulsion potential (U_{elec}) between two colloidal particles of radii a can be expressed as

$$U_{elec}(r) = 2\pi\varepsilon_{0\varepsilon_r}(a+\Delta)\psi_0{}^2 e^{[-\kappa(r-2\Delta-2a)]}, \quad \textbf{(A1)}$$

where ε_r is the permittivity of the medium, Ψ_0 is the potential at the particle surface, which can be estimated from the ξ-potential measurements [40], κ is the inverse Debye length (λ_{Debye}), which is the thickness of the double layer, and Δ is the thickness of the Stern layer. For spherical particles with constant surface potential and the background ionic strength, the van der Waals attraction U_{vdw} between the two particles can be calculated as

$$U_{vdw}(r) = -\frac{A}{6}\left[\frac{2a^2}{r^2-4a^2} + \frac{2a^2}{r^2} + \ln\frac{r^2-4a^2}{r^2}\right], \quad \textbf{(A2)}$$

where A is the Hamaker constant, which is for short-range and plays an important role in describing the attraction energy between particles. Note that the modulus of both potentials (U_{elec} and U_{vdw}) increases when the radii a of the particles increase, which induces a stronger and larger-range interaction between them. When the mean separation distance between particles (r_m), which can be calculated from the concentration by assuming a uniform distribution, is much higher than the particle's hydrodynamic diameter, $D_{Hyd} \approx 2(\lambda_{Debye} + a)$ (extension-range of the repulsive Coulomb potential), a random distribution in the particles position is expected (like an ideal gas). The thickness of the double layer (λ_{Debye}), which must increase with the radii a of the particles, can be determined by the measurement of D_{Hyd} ($\lambda_{Debye} \approx D_{Hyd}/2 - a$). Otherwise, for a r_m similar to or smaller than D_{Hyd}, strong particle interaction is expected, which could lead to a correlation in the particles' positions [35]. The mean electric potential between two neighboring particles is given by the overlap of the repulsive and attractive potentials of the two particles. When λ_{Debye} is of the order of or larger than $h_m/2$, where h_m is the mean distance between the opposite particle surfaces, a sharp secondary minimum of the mean potential is expected. A more uniform distribution or crystallization starts when the colloidal particles fall into this secondary minimum of depth larger than the thermal energy. DLVO theory is not fully effective in describing ordering processes such as the formation of colloidal crystals in suspension and additional interactions should be considered, particularly in water suspensions, where hydrogen bonding and the hydrophobic effect and hydration pressure can play an important role. A detailed work on this topic has been published elsewhere [41,42].

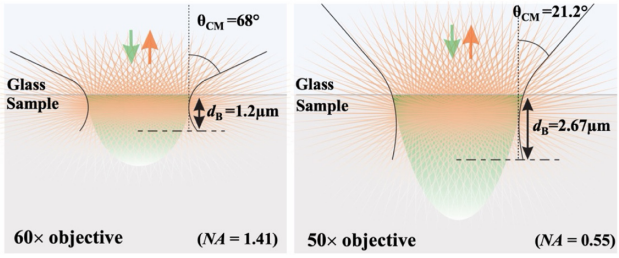

Fig. 5. Illustrations of the processes of pumping and Raman signal collection using the 60× objective (left) with NA = 1.41 and the 50× objective (right) with NA = 0.55. The cone angle, θ_{CM}, and the depth of focus, d_B, are displayed for each setup (60× and 50× objectives). Displayed d_B values correspond to the pumping wavelength of 532 nm.

A.3. Raman Measurements

A Micro-Raman (LabRAM HR Evolution, Horiba Scientific) with four CW lasers (473 nm, 25 mW; 532 nm, 50 mW; 633 nm, 17 mW; and 785 nm, 100 mW) as excitation sources was used for Raman scattering measurements. For these pumping wavelengths, the photon energy is well lower than the bandgap energy of the system (rutile), 3.2 eV (~380 nm), giving rise to non-resonant Raman excitation.

Micro-Raman measurements were done using two objectives, one an oil-immersion Olympus 60× objective with the biggest numerical aperture, NA = 1.41, which translates into a collection depth into the samples of 1.2 μm and another Leica 50× objective with numerical aperture NA = 0.55. Figure 5 shows illustrations of pumping and Raman signal collection at the sample-slide interface using the two objectives (60× and 50×). A total of four spectra, collected from different points, were recorded for each sample. Figure 6 shows normalized Raman spectra collected from the TiO_2@Silica suspension at $FF_{TiO_2} = 0.26\%$, 1.35%, and 12.1% with 50× objective of NA = 0.55. Two strong peaks assigned to the E_g and A_{1g} modes of rutile, located around 445 cm^{-1} and 608 cm^{-1}, are observed. The intensity of these Raman peaks increases quicker than linearly as FF_{TiO_2} is increased above a specific threshold

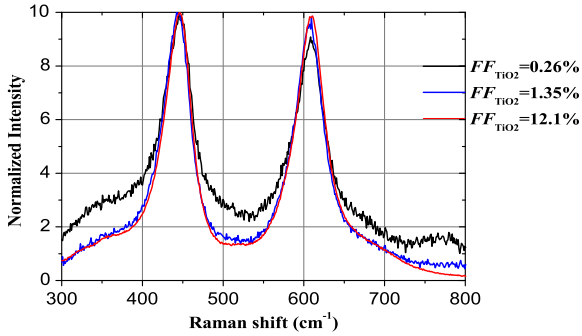

Fig. 6. Raman measurement with 50× objective with NA = 0.55. For FF_{TiO_2} of 0.26%, 1.35%, and 12.1%, Raman spectra collected from the surface of the TiO_2@Silica suspension show the characteristic E_g; 445 cm^{-1} and A_{1g}; 608 cm^{-1} peaks of rutile.

value ($FF_{TiO_2(onset)}$), revealing an enhancement of the Raman signal per particle.

A.4. Correction by Pumping and Collection Depth

The effective pumping intensity (I_{PM}) and collected Raman signal are both affected by the scattering strength (scattering length, l_s) of each sample, which depends on the FF_{TiO_2} and pumping wavelength ($l_{s(\lambda)}$). For correcting the effective pumping intensity by the pumping depth (depth of focus or depth of pumping, d_B), we have taken into account the scattering lengths $l_{s(\lambda)}$ for each sample and pumping wavelength. We considered that the mean pumping intensity ($I_{PM(\lambda)}$) at depth of focus ($d_{B(\lambda)}$) into the sample depends on $l_{s(\lambda)}$ as follows:

$$I_{PM} = \frac{\int_0^{d_{B(\lambda)}} I_P(z)\,dz}{d_{B(\lambda)}} = \frac{I_0}{d_{B(\lambda)}}\int_0^{d_{B(\lambda)}} e^{-\frac{z}{l_{s(\lambda)}}}\,dz$$

$$= -\frac{I_0 l_{s(\lambda)}}{d_{B(\lambda)}}\left(e^{-\frac{d_{B(\lambda)}}{l_{s(\lambda)}}} - 1\right), \tag{A3}$$

where $d_{B(\lambda)}$, $I_P(z)$, and I_0 are the depth of focus and/or collection depth (that depends on the objective and pumping wavelength used), the ballistic pumping intensity at z depth into the sample, and the incident pumping intensity at $z = 0$, respectively. $z = 0$ is at the sample input surface, i.e., at the sample-slide interface (glass). Clearly, when $l_s \gg d_B$, $I_{PM} \approx I_0$. I_0 does not depend on the sample, nor on the pumping wavelength. The collected Raman signal is also the mean of the emitted Raman signal in the collection depth, which is the same as the pumping depth. Therefore, in order to correct the collected Raman intensity (I_{CR}), the measured Raman signal is divided by $[-\frac{l_{s(\lambda)}}{d_{B(\lambda)}}(e^{-\frac{d_{B(\lambda)}}{l_{s(\lambda)}}} - 1)]^2$ for each sample and specific pumping wavelength, considering pumping and collection. The position of the objective focus relative to the sample surface was chosen experimentally such that the maximum Raman signal was obtained. This implies that the effective depth of pumping and collection could be slightly less than the depth of focus of the objective (d_B). Additionally, for the pumping and collection with the 50× objective, we must include a correction for the reflected pumping light at the air-slide and slide-sample interfaces, and the reflection of the emitted light at the slide-air interface (non-index matching). Therefore, the measured Raman signal must also be divided by $\langle 1 - \mathrm{Ref}_{CM}\rangle$, where Ref_{CM} is the average reflection coefficient between 0° and θ_{CM} at the above interfaces.

A.5. Scattering Strength and l_s Values as a Function of the Pumping Wavelength

In order to rule out a classical interferential phenomenon, the Raman signal for FF_{TiO_2} of 4.8% and 8.8% and $FF_{SiO_2} = 0.75\%$ was studied by using four different pumping wavelengths (473 nm, 532 nm, 633 nm, and 785 nm) with the 50× objective. For FF_{TiO_2} of 4.8% and 8.8%, the scattering strength and l_S were calculated by Mie theory taking into account the l_S value at $FF_{TiO_2} = 4.8\%$ (1.15 μm) determined experimentally using 532 nm. Figure 7(a) shows the scattering strength for $FF_{TiO_2} = 4.8\%$ as a function of the wavelength. The scattering strength values at the four pumping wavelengths are indicated on the curve by arrows. Figure 7(b) shows the scattering length (l_S) for the four pumping wavelengths (473 nm, 532 nm, 633 nm, and 785 nm) at FF_{TiO_2} of 4.8% and 8.8%.

Funding. Office of Naval Research (N00014-20-1-2789); Comissão Nacional de Energia Nuclear (2020.06.IPEN.33.PD); Conselho Nacional de Desenvolvimento Científico e Tecnológico (313703/2021-3, 435260/2018-9, 465423/2014-0); Fundação de Amparo À Pesquisa do Estado de São Paulo (2017/10765-5, 2017/11986-5, 2018/19240-5, 2019/06334-4, 2021/04334-7)2022/02525-2).

Acknowledgment. We appreciate useful support of Professor Weliton Martins. We extend additional thanks to designer Pedro Silva for the graphical image. F.C.M. and E.J.V. synthesized nanoparticles, J.D., N.U.W., and E.J.V. performed the Raman experiments, J.D., N.U.W., F.C.M., A.Z.F., A.D., and E.J.V. analyzed the results and prepared the manuscript, and E.J.V. wrote the manuscript and guided the research.

Disclosures. The authors declare no conflicts of interest.

Data availability. Data underlying the results presented in this paper are not publicly available at this time but may be obtained from the authors upon reasonable request.

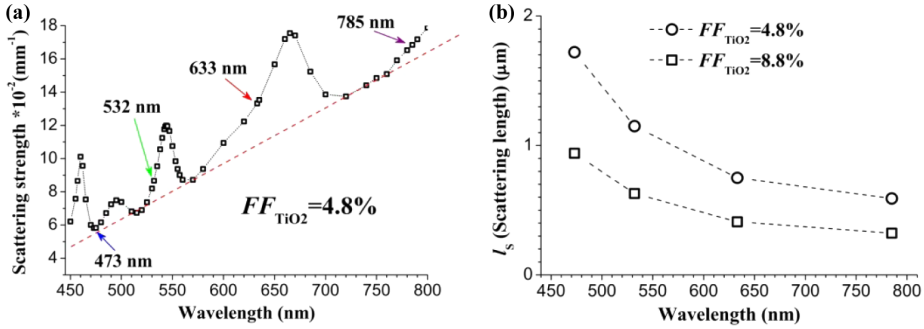

Fig. 7. Scattering strength and l_S, calculated by Mie theory. (a) Scattering strength for $FF_{TiO_2} = 4.8\%$ as a function of wavelength. Scattering strength values at the pump wavelengths of 473 nm, 532 nm, 633 nm, and 785 nm are indicated by the blue, green, red, and brown arrows, respectively. (b) FF_{TiO_2} of 4.8% and 8.8%, l_S values, determined by Mie theory and scaled by $l_S = 1.15$ μm value measured experimentally at $FF_{TiO_2} = 4.8\%$, are displayed for the four pumping wavelengths (473 nm, 532 nm, 633 nm, and 785 nm). The dashed lines are just to join the l_S values on the curve.

REFERENCES

1. X. Bi, D. M. Czajkowsky, Z. Shao, *et al.*, "Digital colloid-enhanced Raman spectroscopy by single-molecule counting," Nature **628**, 771–775 (2024).
2. S. Nie and S. R. Emory, "Probing single molecules and single nanoparticles by surface-enhanced Raman scattering," Science **275**, 1102–1106 (1997).
3. K. Kneipp, Y. Wang, H. Kneipp, *et al.*, "Single molecule detection using surface-enhanced Raman scattering (SERS)," Phys. Rev. Lett. **78**, 1667 (1997).
4. J. Homola, "Present and future of surface plasmon resonance biosensors," Anal. Bioanal. Chem. **377**, 528–539 (2003).
5. G. Fuertes, O. L. Sánchez-Muñoz, E. Pedrueza, *et al.*, "Switchable bactericidal effects from novel silica-coated silver nanoparticles mediated by light irradiation," Langmuir **27**, 2826–2833 (2011).
6. G. Fuertes, E. Pedrueza, K. Abderrafi, *et al.*, "Photoswitchable bactericidal effects from novel silica-coated silver nanoparticles," Proc. SPIE **8092**, 80921M (2011).
7. D. P. O'Neal, L. R. Hirsch, N. J. Halas, *et al.*, "Photo-thermal tumor ablation in mice using near infrared-absorbing nanoparticles," Cancer Lett. **209**, 171–176 (2004).
8. M. A. Noginov, G. Zhu, A. M. Belgrave, *et al.*, "Demonstration of a spaser-based nanolaser," Nature **460**, 1110–1112 (2009).
9. M. A. Noginov, G. Zhu, M. Mayy, *et al.*, "Stimulated emission of surface plasmon polaritons," Phys. Rev. Lett. **101**, 1–4 (2008).
10. M. Jahn, S. Patze, I. J. Hidi, *et al.*, "Plasmonic nanostructures for surface enhanced spectroscopic methods," Analyst **141**, 756–793 (2016).
11. D. S. Wiersma, P. Bartolini, A. Lagendijk, *et al.*, "Localization of light in a disordered medium," Nature **390**, 671–673 (1997).
12. M. Störzer, P. Gross, C. M. Aegerter, *et al.*, "Observation of the critical regime near Anderson localization of light," Phys. Rev. Lett. **96**, 063904 (2006).
13. F. Scheffold, R. Lenke, R. Tweer, *et al.*, "Localization or classical diffusion of light?" Nature **398**, 206–207 (1999).
14. F. Scheffold and D. Wiersma, "Inelastic scattering puts in question recent claims of Anderson localization of light," Nat. Photonics **7**, 934 (2013).
15. T. Van Der Beek, P. Barthelemy, P. M. Johnson, *et al.*, "Light transport through disordered layers of dense gallium arsenide submicron particles," Phys. Rev. B **85**, 115401 (2012).
16. T. Sperling, L. Schertel, M. Ackermann, *et al.*, "Can 3D light localization be reached in 'white paint'?" New J. Phys. **18**, 13039 (2016).
17. S. E. Skipetrov and I. M. Sokolov, "Absence of Anderson localization of light in a random ensemble of point scatterers," Phys. Rev. Lett. **112**, 023905 (2014).
18. S. John, "Strong localization of photons in certain disordered dielectric superlattices," Phys. Rev. Lett. **58**, 2486–2489 (1987).
19. P. A. Nosov, I. M. Khaymovich, and V. E. Kravtsov, "Correlation-induced localization," Phys. Rev. B **99**, 104203 (2019).
20. S. John, "Electromagnetic absorption in a disordered medium near a photon mobility edge," Phys. Rev. Lett. **53**, 2169–2172 (1984).
21. S. John and J. Wang, "Quantum optics of localized light in a photonic band gap," Phys. Rev. B **43**, 12772–12789 (1991).
22. F. Sgrignuoli, S. Torquato, and L. Dal Negro, "Subdiffusive wave transport and weak localization transition in three-dimensional stealthy hyperuniform disordered systems," Phys. Rev. B **105**, 064204 (2022).
23. O. J. Trojak, S. Gorsky, C. Murray, *et al.*, "Cavity-enhanced light–matter interaction in Vogel-spiral devices as a platform for quantum photonics," Appl. Phys. Lett. **118**, 011103 (2021).
24. S. Yu, C.-W. Qiu, Y. Chong, *et al.*, "Engineered disorder in photonics," Nat. Rev. Mater. **6**, 226–243 (2020).
25. K. Vynck, R. Pierrat, R. Carminati, *et al.*, "Light in correlated disordered media," Rev. Mod. Phys. **95**, 045003 (2023).
26. S. Torquato, "Extraordinary disordered hyperuniform multifunctional composites," J. Compos. Mater. **56**, 3635–3649 (2022).
27. S. Yu, "Evolving scattering networks for engineering disorder," Nat. Comput. Sci. **3**, 128–138 (2023).
28. E. Jimenez-Villar, V. Mestre, P. C. de Oliveira, *et al.*, "Novel core–shell (TiO2@Silica) nanoparticles for scattering medium in a random laser: higher efficiency, lower laser threshold and lower photodegradation," Nanoscale **5**, 12512 (2013).
29. E. Jimenez-Villar, V. Mestre, P. C. de Oliveira, *et al.*, "TiO2@Silica nanoparticles in a random laser: Strong relationship of silica shell thickness on scattering medium properties and random laser performance," Appl. Phys. Lett. **104**, 081909 (2014).
30. E. Jimenez-Villar, I. F. Da Silva, V. Mestre, *et al.*, "Anderson localization of light in a colloidal suspension (TiO2@silica)," Nanoscale **8**, 10938–10946 (2016).
31. E. Jimenez-Villar, V. Mestre, W. S. Martins, *et al.*, "Core-shell TiO2@Silica nanoparticles for light confinement," Mater. Today Proc. **4**(11), 11570–11579 (2017).
32. E. Jiménez-Villar, I. F. da Silva, V. Mestre, *et al.*, "Random lasing at localization transition in a colloidal suspension (TiO2@Silica)," ACS Omega **2**, 2415–2421 (2017).
33. E. Jimenez-Villar, M. C. S. Xavier, J. G. G. S. Ramos, *et al.*, "Localization of light: beginning of a new optics," Proc. SPIE **10549**, 1054905 (2018).
34. E. Jimenez-Villar, M. C. S. Xavier, N. U. Wetter, *et al.*, "Anomalous transport of light at the phase transition to localization: strong dependence with incident angle," Photonics Res. **6**, 929 (2018).
35. V. A. Ermakov, W. S. Martins, N. U. Wetter, *et al.*, "Localization of light induced in ordered colloidal suspensions: powerful sensing tools," Nanoscale **13**, 6417–6425 (2021).
36. C. T. Dominguez, A. A. V. Gomes, N. U. Wetter, *et al.*, "Random lasing at localization induced in correlated colloidal system," Opt. Mater.-Amsterdam **120**, 111428 (2021).
37. E. Jiménez-Villar, W. S. Martins, and N. U. Wetter, "Ordered photonic colloidal suspensions," Appl. Opt. **62**, 2707 (2023).
38. F. Sgrignuoli, R. Wang, F. A. Pinheiro, *et al.*, "Localization of scattering resonances in aperiodic Vogel spirals," Phys. Rev. B **99**, 104202 (2019).
39. R. J. Hunter, *Foundations of Colloid Science*, 2nd ed. (Oxfort University, 2001).
40. D. Bastos and F. J. de las Nieves, "Colloidal stability of sulfonated polystyrene model colloids. Correlation with electrokinetic data," Colloid Polym. Sci. **272**, 592–597 (1994).
41. N. Ise and I. S. Sogami, *Structure Formation in Solution: Ionic Polymers and Colloidal Particles* (Springer, 2005).
42. L. Bressel, R. Hass, and O. Reich, "Particle sizing in highly turbid dispersions by photon density wave spectroscopy," J. Quant. Spectrosc. Radiat. Transf. **126**, 122–129 (2013).